iScience

CellPress
OPEN ACCESS

Article

Spontaneous Fe^{III}/Fe^{II} redox cycling in single-atom catalysts: Conjugation effect and electron delocalization

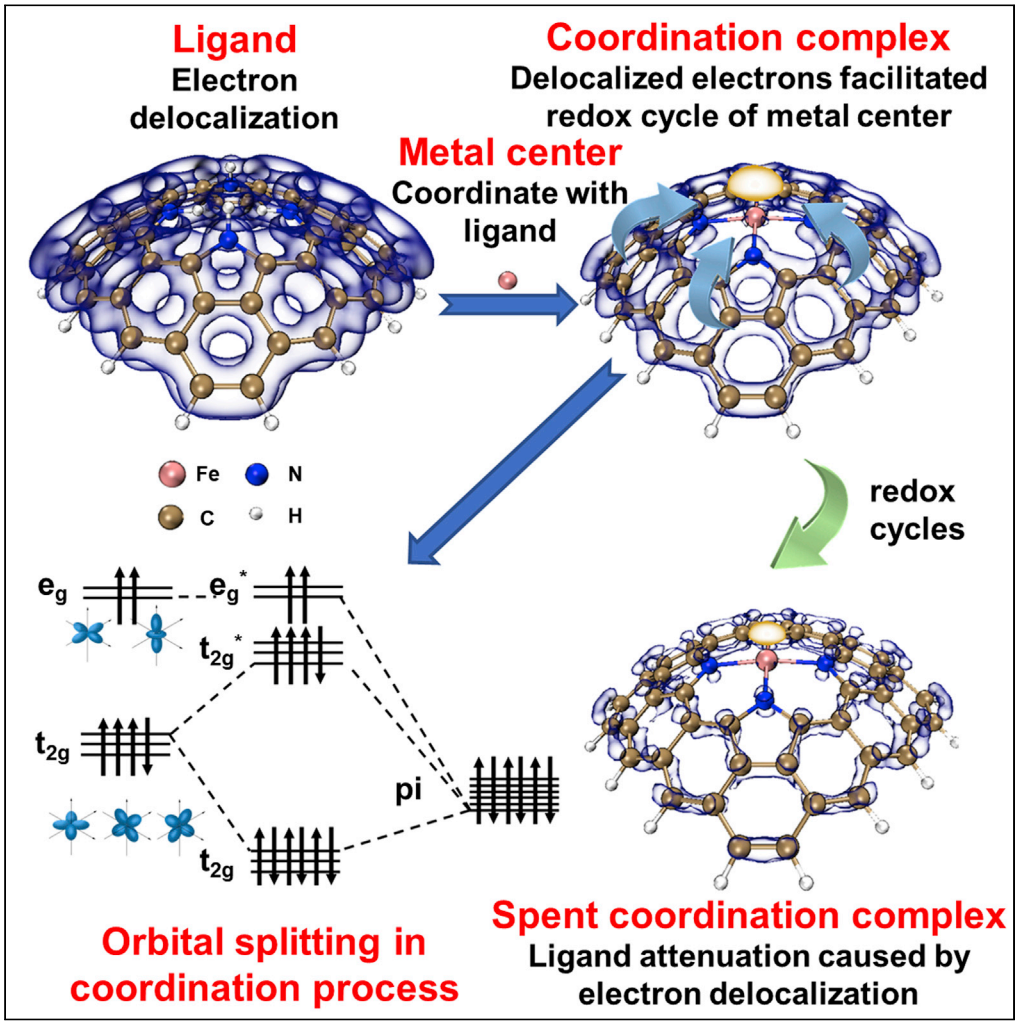

Zheng Qian, Lingzhen Wang, Mawuli Dzakpasu, ..., Rongzhi Chen, Gen Wang, Shengjiong Yang

crz0718@ucas.ac.cn (R.C.)
yangshengjiong@163.com (S.Y.)

Highlights

The electronic behavior of single-atom catalyst was investigated by ligand-field theory

Delocalized electron in ligand of single-atom catalyst facilitated Fe^{III}/Fe^{II} redox cycle

Radical pathway could not be maintained for long time due to the attenuation of ligand

Qian et al., iScience 26, 105902
January 20, 2023
https://doi.org/10.1016/j.isci.2022.105902

iScience

CellPress
OPEN ACCESS

Article

Spontaneous Fe^{III}/Fe^{II} redox cycling in single-atom catalysts: Conjugation effect and electron delocalization

Zheng Qian,[1] Lingzhen Wang,[1] Mawuli Dzakpasu,[1] Yujia Tian,[1] Dahu Ding,[2] Rongzhi Chen,[3,*] Gen Wang,[1] and Shengjiong Yang[1,4,*]

SUMMARY

The mechanism of spontaneous Fe^{III}/Fe^{II} redox cycling in iron-centered single-atom catalysts (I-SACs) is often overlooked. Consequently, pathways for continuous $SO_4^{\cdot-}$/HO· generation during peroxymonosulfate (PMS) activation by I-SACs remain unclear. Herein, the evolution of the iron center and ligand in I-SACs was comprehensively investigated. I-SACs could be considered as a coordination complex created by iron and a heteroatom N-doped carbonaceous ligand. The ligand-field theory could well explain the electronic behavior of the complex, whereby electrons delocalized by the conjugation effect of the ligand were confirmed to be responsible for the Fe^{III}/Fe^{II} redox cycle. The possible pyridinic ligand in I-SACs was demonstrably weaker than the pyrrolic ligand in Fe^{III} reduction due to its shielding effect on delocalized π orbitals by local lone-pair electrons. The results of this study significantly advance our understanding of the mechanism of spontaneous Fe^{III}/Fe^{II} redox cycling and radical generation pathways in the I-SACs/PMS process.

INTRODUCTION

Heteroatom doping has been widely conducted to regulate the inertness of carbon-based materials for better catalytic activity.[1–8] Due to the differences in the electronegativity between C and heteroatoms, non-metal heteroatom doping, such as N, could create positively charged sites on the negative carbon matrix, rendering a rearrangement of the electronic structure for effective peroxymonosulfate (PMS) activation.[9] Recently, atomically dispersed metal sites on the carbon matrix, also known as single-atom catalysts (SACs), have received increasing attention because of their high activity in various fields.[10–17] Burgeoning studies also proposed that SACs were effective in PMS activation. Non-radical-dominated mechanism was widely accepted to contribute primarily to organic pollutants degradation when N-doped carbon was used for PMS activation.[10,11,18] However, when it comes to SACs, it was demonstrated that both radical and non-radical pathways were involved.[19,20] The radical pathway of PMS activation usually acquires external energy or a metallic electron donor, such as heat/radiation or transition metal.[21] Against this background, Co was deemed the optimum catalyst for the generation of radicals due to the spontaneous Co^{III}/Co^{II} redox cycle when it coexists with PMS .[22] Fe is another widely used environmentally friendly catalyst for PMS activation. However, the PMS activation performance of Fe is largely limited because of the inefficient Fe^{III}/Fe^{II} redox cycle. Various efforts have been made to solve this problem. For example, the photo-Fenton process significantly facilitated the Fe^{3+}/Fe^{2+} (Fe^{n+}, n = +2, +3, represents free Fe cations in bulk solution) redox cycle for better pollutant degradation.[23] Hydroxylamine was also proved to be effective in Fe^{2+} generation in Fenton-like processes due to its strong reducibility.[24] It is, thus, demonstrated that external energy or a chemical reductant is always required. Interestingly, when iron was used as the metal center in SACs (I-SACs), the continuous generation of radicals suggested a spontaneous Fe^{III}/Fe^{II} (Fe^{III} and Fe^{II} represent trivalent and bivalent Fe species anchored on the surface of solid phase, respectively) redox cycling. However, elucidation of the mechanism of PMS activation by I-SACs usually focused on the synergism of the dual active sites (iron center and adjacent N sites).[25] Explanations for the spontaneous Fe^{III}/Fe^{II} redox cycle were invariably ignored.

Notably, the carbon matrix is rich in π electrons with a conjugated structure. Due to the conjugation effect of the carbon matrix, the π electrons are highly delocalized in ligands. Considering the coordination

[1]School of Environmental and Municipal Engineering, Xi'an University of Architecture and Technology, No. 13, Yanta Road, Xi'an, Shaanxi 710055, China

[2]College of Resources and Environmental Sciences, Nanjing Agricultural University, No. 1, Weigang, Nanjing, Jiangsu 210095, China

[3]College of Resources and Environment, University of Chinese Academic of Science, 19A Yuquan Road, Beijing, 100049, China

[4]Lead contact

*Correspondence: crz0718@ucas.ac.cn (R.C.), yangshengjiong@163.com (S.Y.)

https://doi.org/10.1016/j.isci.2022.105902

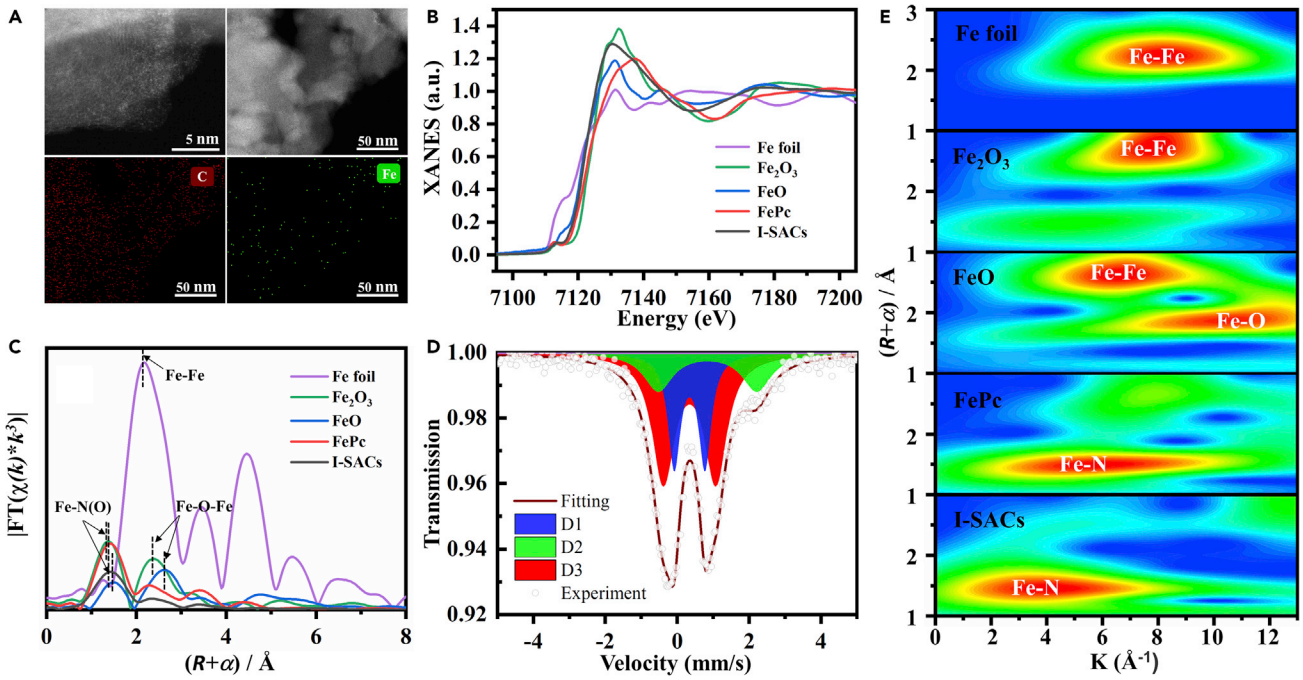

Figure 1. Distribution and chemical environment of Fe in I-SACs

(A) HAADF-STEM image and EDS mapping of I-SACs.

(B) Normalized Fe K-edge XANES spectra of Fe foil, Fe_2O_3, FeO, FePc, and I-SACs.

(C) k^3-weighted Fourier transform spectra from the Fe k-edge EXAFS for Fe foil, Fe_2O_3, FeO, FePc, and I-SACs without correcting phase.

(D) ^{57}Fe Mössbauer spectra of I-SACs at room temperature.

(E) Wavelets of Fe foil, Fe_2O_3, FeO, FePc, and I-SACs.

between iron and ligand provided a possible explanation for Fe^{III}/Fe^{II} redox cycling during the I-SACs/PMS process, which is very important in understanding the mechanism of iron center redox cycling for PMS activation. In addition, the pyridinic ligand has been widely used as an acquiescent ligand in I-SACs to investigate its chemical behavior in various density functional theory studies.[26–28] However, pyrrolic ligands might also coordinate with iron in I-SACs, considering the widely existing benchmark chemicals containing pyrrolic N-Fe bonds, such as iron(II) phthalocyanine (FePc) and iron porphyrin. Hitherto, the effects of pyridinic and pyrrolic ligands on the catalytic performance of I-SACs are still lacking attention, and inceptive investigation is needed.

This study carefully explored the electronic structure and chemical properties of I-SACs during the PMS activation process. The influences of various reaction conditions, identification of reactive oxidation species (ROS), the mechanism of PMS activation by I-SACs, and the difference between pyridinic and pyrrolic ligands in I-SACs were systematically explored. More importantly, a theoretical conclusion with respect to the redox cycling of the iron center in single-atom catalysts was firstly proposed to provide new insights into the mechanism of PMS activation by iron-centered single-atom catalysts.

RESULTS AND DISCUSSION

Characterization of catalyst

Field emission scanning electron microscopy image of I-SACs in Figure S1A shows uniformly distributed Fe sites on the surface of I-SACs. The abundance of Fe is largely lower than N and C, corroborating well with energy dispersive spectroscopy analysis (Figure S1B). High-angle annular dark-field scanning TEM (HAADF-STEM) image of I-SACs (Figure 1A) exhibits individually dispersed bright sites on the surface of the sample. Element mapping revealed that the highly dispersed bright sites were atomic Fe. In addition, a slightly dispersed ultrafine Fe cluster could also be observed in the HAADF-STEM image. Coordination complexes formed by Fe cations and 1,10-phenanthroline is effective in separating one iron site from another and preventing the agglomeration of iron sites during pyrolysis treatment due to the comparative

thermal stability of 1,10-phenanthroline. Therefore, single atomic iron sites on the carbon support could be formed.[29–31] However, the evaporation of nitrogen from the carbon support is inevitable during the pyrolysis treatment, which caused the formation of slightly agglomerated single atomic iron sites. Therefore, Fe clusters were slightly generated during the synthesis of the catalyst, which might facilitate the adsorption performance toward anions.[32] Figure S1C presents X-ray diffraction curves of the catalysts, where two peaks with large widths centered around 24.70° (2θ) and 43.70° (2θ) could be attributed to the amorphous carbon (002) and crystalline carbon (100).[33] A Fe-containing crystalized phase was absent throughout the pattern, further proving the size of the clusters is very small. X-ray photoelectron spectroscopy (XPS) analysis identified the chemical composition on the surface of all samples (Figure S1G and Table S1). Inductively coupled plasma mass spectrometry analysis evidenced that the content of Fe in I-SACs is about 1.42% (wt %). The Fe $2p_{3/2}$ XPS spectrum of I-SACs was located at 711.6 eV, possibly indicating the coexistence of Fe^{II} and Fe^{III} species (Figure S1H). Furthermore, the result showed that the binding energy of Fe $2p_{3/2}$ shifted to about 711.0 eV after Ar etching, indicating that divalent Fe significantly dominated in I-SACs. The O 1s spectrum exhibits slight existence of Fe-*O*-Fe species (530.4 eV), which amounted to 0.75%. Moreover, C=O (531.8 eV) and -OH (533.5 eV) could also be observed in the atomic concentrations of 0.93% and 3.22%, respectively. The N content in I-SACs mainly existed as pyridinic N (399.1 eV), Fe-N (399.8 eV), pyrrolic N (400.8 eV), and graphitic N (402.0 eV) because of the pyrolysis of nitrogen source (1,10-phenanthroline) in the precursor.[34] As discussed above, the normal carbon framework (hexagonal topological carbon structure) usually exhibited electronic inertness, rendering low catalytic performance. The successfully doped Fe and N would modulate the electronic structure of the carbon framework, facilitating its catalytic activity through electron rearrangement.

The Raman spectrum (Figure S1D) manifested two peaks at 1580 and 1360 cm^{-1}, corresponding to graphitization of sp^2 carbon (G band) and disordered carbon (D band), respectively,[35] corroborating the theoretical Raman spectra (Figures S2A–S2F). The intensity ratio of D versus G (I_D/I_G = 1.09) demonstrated that defects might be created through the carbonization of the $[Fe(1,10\text{-phenanthroline})_3]^{2+}$ complex. Fourier transform infrared spectroscopy (FT-IR) spectrum suggested three peaks located at 3440, 3240, and 1630 cm^{-1} (Figure S1E). According to the deciphering of the corresponding theoretical IR spectrum, the weak peak positioned at 3240 cm^{-1} could be assigned to the stretching vibration of C-H at the edge of the carbon framework (Figures S2H and S2K). Also, the peaks at 1630 cm^{-1} could be assigned to the stretching vibration of the graphitic carbon framework (Figure S2I and S2L). The strong peak located at 3440 cm^{-1} could be regarded as -OH due to the existence of moisture and surface hydroxyl group. N_2 adsorption-desorption analysis revealed that the Brunauer-Emmett-Teller surface area of the catalysts is 48 m^2/g with a type-III adsorption isotherm (Figure S1F). The occurrence of an adsorption-desorption hysteresis at P/P_0 of 0.8 demonstrated the coexistence of mesopore and macropore,[36] which can be proved with pore width distribution analysis (24–32 nm, Table S1).

Extended X-ray absorption fine structure (EXAFS) and X-ray absorption near-edge structure (XANES) were conducted to confirm the chemical states and local environment of Fe. The Fe K-edge XANES spectra of I-SACs (Figure 1B) were located between FeO and Fe_2O_3, indicating that the valence of Fe in samples ranged between +2 and +3. Figure 1C illustrates the Fourier transform (FT) k^3-weighted EXAFS spectrum in R space. Fe-Fe bond at ~2.2 Å could not be observed by comparison with the result of Fe foil. A peak located at ~1.5 Å could be assignable to the Fe-N scattering path. The least-square fitting analysis of EXAFS demonstrated that the first shell of the Fe atom in I-SACs is coordinated with 4 N atoms (Figure S3D and Table S2). Meanwhile, a peak with very low intensity was located at ~2.4 Å in EXAFS of I-SACs, which is similar to Fe-*O*-Fe. Therefore, the existence of a few oxidized Fe clusters could be confirmed in the sample, corroborating the findings of the HAADF-STEM analysis. The wavelet transform (Figure 1E) results show a maximum intensity at about 4.3 $Å^{-1}$, which is very close to that of FePc (~5.4 $Å^{-1}$) but highly differed from that of Fe foil (8.2 $Å^{-1}$). This result underlined the Fe-N coordination environment, further proving the atomic dispersion of Fe atoms.[37]

In addition, the states of the Fe-N_x moieties in I-SACs were further confirmed by ^{57}Fe Mössbauer spectra (Figure 1D and Table S3). The spectrum could be well fitted with three doublets, D1, D2, and D3, with relative contents of 26.8%, 21.0%, and 52.2%, respectively. The values of isomer shift (IS) and Q splitting (QS) for D1 (IS = 0.34 mm/s, QS = 0.85 mm/s) were typically deemed as a Fe center in Fe^{II}-N_4-C. However, it was also reported by Bouwkamp-Wijnoltz[38] that an IS = 0.37 mm/s and QS = 0.96 mm/s might be a Fe center in the Fe^{III}-N_4-C structure. D2 (IS = 0.84 mm/s, QS = 2.74 mm/s) has been widely observed and recently identified

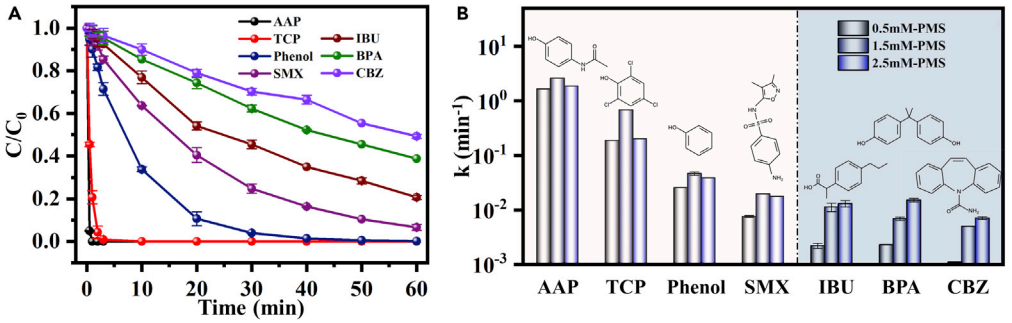

Figure 2. Oxidation performance of the I-SACs/PMS system

(A) Degradation of various contaminants in the I-SACs/PMS system ([I-SACs] = 0.1 g L^{-1}, [AAP] = [TCP] = [Phenol] = [SMX] = [IBU] = [BPA] = [CBZ] = 50 μM, [PMS] = 1.5 mM, [pH] = 6.8 ± 0.1, [Temperature] = 25 ± 0.3°C).

(B) K_{obs} of different contaminants degradation in the I-SACs/PMS system under different PMS concentrations ([I-SACs] = 0.1 g L^{-1}, [AAP] = [TCP] = [Phenol] = [SMX] = [IBU] = [BPA] = [CBZ] = 50 μM, [PMS] = 0.5–2.5 mM, [pH] = 6.8 ± 0.1, [Temperature] = 25 ± 0.3°C).

as Fe^{II}-N_4-C,[39] and D3 (IS = 0.34 mm/s, QS = 1.46) could be assigned to a high spin Fe^{II}-N_4.[25,39,40] Therefore, Fe^{II} was the dominant species in I-SACs.

Oxidation performance of the catalyst

Several refractory organic pollutants were used as representative pollutants to investigate the oxidation performance of the I-SACs/PMS process. Figure 2A demonstrates that 4-acetaminophen (AAP), trichlorophenol (TCP), and phenol could be completely degraded within 50 min. Furthermore, sulfamethoxazole (SMX), ibuprofen (IBU), bisphenol-A (BPA), and carbamazepine (CBZ) could also be degraded with lower degradation efficiency. The degradation efficiency usually depended on the concentration of coexisted PMS. The degradation reaction rate of AAP, TCP, phenol, and SMX peaked at a PMS concentration of 1.5 mM. Furthermore, increased PMS concentration (2.5 mM) significantly inhibited the degradation rate (Figure 2B), which is reminiscent of the quenching reaction of radical/radical and radical/PMS. This result implied the existence of a radical-involved pathway during the activation reaction.[41] On the contrary, increased PMS concentration significantly elevated the degradation performance toward IBU, BPA, and CBZ. The absence of a negative effect of excessive PMS suggested pollutant degradation by the electron transfer process caused by the surface-activated PMS.[17,42] By using AAP as an example, increasing the initial pH inhibited the AAP degradation, with a decrease in the reaction rate to its lowest of 0.07 min^{-1} at the initial pH of 9.67 (Figure S4A). The zero-point charge of I-SACs was measured as 4.4 (Figure S4A inset), indicating a positively charged surface in solution with a pH lower than 4.4. On the contrary, the surface of the catalyst was negative in higher pH solutions. The electrostatic repulsion between the negatively charged catalyst surface and PMS anions inhibited the PMS activation under alkaline solution. The leaching of Fe cations during PMS activation was only 0.37 μg L^{-1}, which accounts for 0.002% of the total Fe in the catalyst. Thus, the heterogeneous, rather than homogeneous catalytic behavior of the I-SACs/PMS process could be confirmed.

Identification of reactive oxidation species

The ROS involved in the oxidation reaction were identified to elucidate the mechanism. Methanol (Meth) was used to quench $SO_4^{\cdot-}$ and HO• ($k_{SO_4^{\cdot-},meth}$ = 1.1 × 10^7 M^{-1} s^{-1} and $k_{HO\cdot,meth}$ = 9.7 × 10^8 M^{-1} s^{-1}), whereas tertiary butyl alcohol (TBA) was used as a typical quencher toward HO• ($k_{HO\cdot,TBA}$ = 7.6 × 10^8 M^{-1} s^{-1}).[43] As shown in Figure 3A, Meth exhibited significant inhibition, and the reaction rate decreased from 0.95 (w/o quencher) to 0.19 min^{-1}. TBA also exhibited notable inhibition, with a reaction rate of 0.17 min^{-1}, suggesting $SO_4^{\cdot-}$ and HO• were widely generated in the I-SACs/PMS process. Electron paramagnetic resonance (EPR) analysis further revealed that both $SO_4^{\cdot-}$ and HO• could be identified (Figure 3B) by using 5,5-dimethyl-1-pyrolin-N-oxide as a spin-trapping agent,[44] suggesting the cleavage of O-O bonds in PMS. The instant signal intensity decreased with reaction time, possibly indicating a gradual decrease in radical generation. On the other hand, benzoic acid (BA) was always used as an effective probe toward $SO_4^{\cdot-}$ and HO• because BA could be rapidly oxidized to *p*-hydroxybenzoic acid (*p*-HBA) by $SO_4^{\cdot-}$ and HO• ($k_{SO_4^{\cdot-},BA}$ = 1.2 × 10^9 $M^{-1}s^{-1}$ and $k_{HO\cdot,BA}$ = 6.0 × 10^9 $M^{-1}s^{-1}$).[45] As shown in Figure 3C, about 61% of BA (30.5 μM) was degraded, and about 2.65 μM of *p*-HBA was generated simultaneously in the

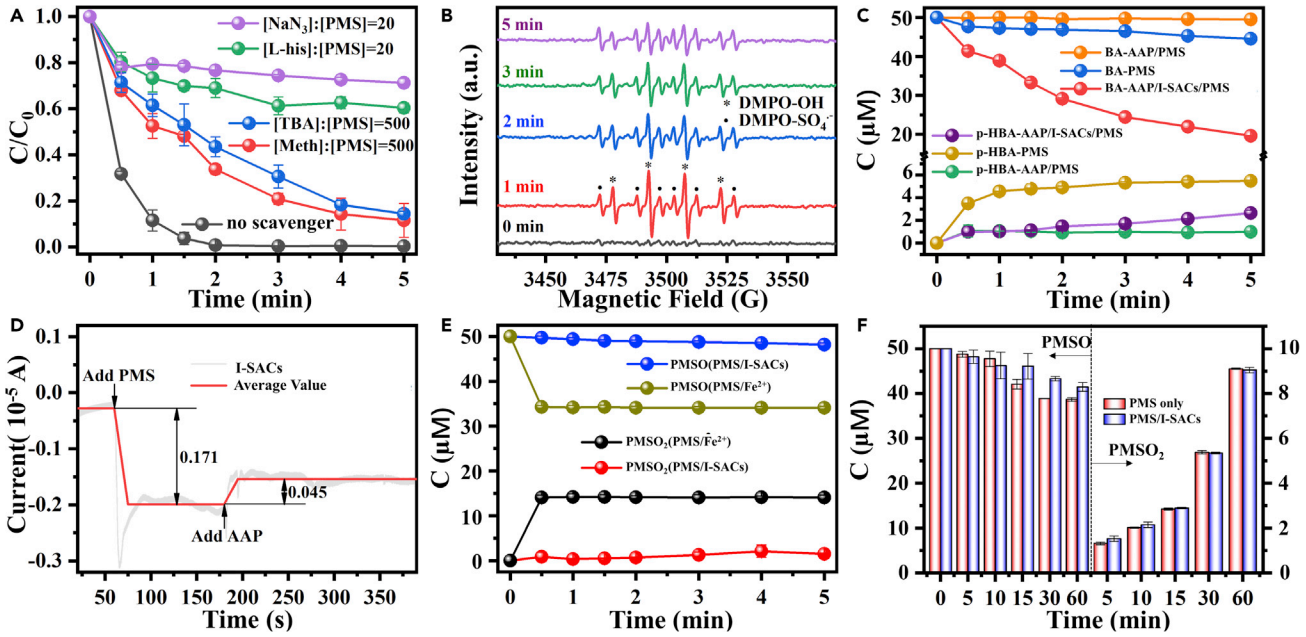

Figure 3. Identification of reactive active species in the I-SACs/PMS system

(A) Degradation of AAP in the presence of different scavengers in the I-SACs/PMS system ([I-SACs] = 0.1 g L^{-1}, [AAP] = 100 μM, [PMS] = 0.5 mM, [pH] = 6.8 ± 0.1, [Temperature] = 25 ± 0.3°C).

(B) Time evolution of EPR signal by using DMPO spin-trapping agents ([I-SACs] = 0.1 g L^{-1}, [PMS] = 0.5 mM, [DMPO] = 90 μM, [pH] = 6.8 ± 0.1, [Temperature] = 25 ± 0.3°C).

(C) BA degradation and *p*-HBA generation in the I-SACs/PMS system ([I-SACs] = 0.1 g L^{-1}, [AAP] = 100 μM, [PMS] = 0.5 mM, [BA] = 50 μM, [pH] = 6.8 ± 0.1, [Temperature] = 25 ± 0.3°C).

(D) I-t curve of the I-SACs/PMS system, the fluctuation was presented by average value ([I-SACs] = 0.2 mg/cm^2, [AAP] = 100 μM, [PMS] = 0.5 mM, [pH] = 6.8 ± 0.1, [Na_2SO_4] = 0.1 M, [Temperature] = 25 ± 0.3°C, [Init E] = 0.3 V, [Sample interval] = 0.1 s, [Run time] = 400 s, [Quiet time] = 0 s, [Sensitivity] = 10^{-6} A/V).

(E) PMSO degradation and $PMSO_2$ generation in the I-SACs/PMS system ([I-SACs] = 0.1 g L^{-1}, [AAP] = 100 μM, [PMS] = 0.5 mM, [PMSO] = 50 μM, [pH] = 6.8 ± 0.1, [Temperature] = 25 ± 0.3°C).

(F) Comparison of PMSO degradation and $PMSO_2$ generation in PMS/PMSO system and I-SACs/PMS/PMSO system ([I-SACs] = 0.1 g L^{-1}, [AAP] = 100 μM, [PMS] = 0.5 mM, [PMSO] = 50 μM, [pH] = 6.8 ± 0.1, [Temperature] = 25 ± 0.3°C).

AAP/I-SACs/PMS process. By comparison, the degradation of BA and generation of *p*-HBA by the PMS solution were 5.42 and 5.49 μM, respectively. This result indicates a strong oxidation performance of the system, which not only transforms BA into *p*-HBA through hydroxylation but also largely degraded the generated *p*-HBA.

Furthermore, NaN_3 and L-histidine (L-his), the commonly accepted scavengers for $^1O_2$ elimination ($k_{1_{O_2,NaN_3}} = 2 \times 10^9 M^{-1}s^{-1}$ *and* $k_{1_{O_2,L-his}} = 9.7 \times 10^8 M^{-1}s^{-1}$), exhibited stronger inhibition toward organic degradation.[46] EPR analysis further evidenced the triplet signal by using 2,2,6,6-tetramethylpiperidine as a trapping agent, representing the generation of $^1O_2$ (Figure S5A). The signal intensity largely increased with increasing reaction time, indicating that $^1O_2$ was widely generated in the I-SACs/PMS reaction. Furthermore, the $^1O_2$ signal obtained in I-SACs/PMS with argon aeration was weaker than that in the I-SACs/PMS system (Figure S5B). Also, the degradation rate sharply decreased accordingly (Figure S5C), demonstrating that $^1O_2$ also contributed to organic degradation.

Elevated IBU, BPA, and CBZ degradation under excessive PMS suggested that the electron transfer from organic to surface-activated PMS (PMS*) might be also a possible pathway for pollutant degradation.[47] To explore whether the electron transfer was involved, the electrochemical behavior of the I-SACs/PMS system was evaluated. Open-circuit potential analysis (Figure S5D) exhibited the increase of surface potential once PMS was added into the solution in all groups, indicating that PMS in solution was adsorbed on the surface of the working electrode coated with I-SACs. According to the previous literature, Fe clusters in the catalyst might play a non-innocent role toward anion adsorption even though these clusters themselves

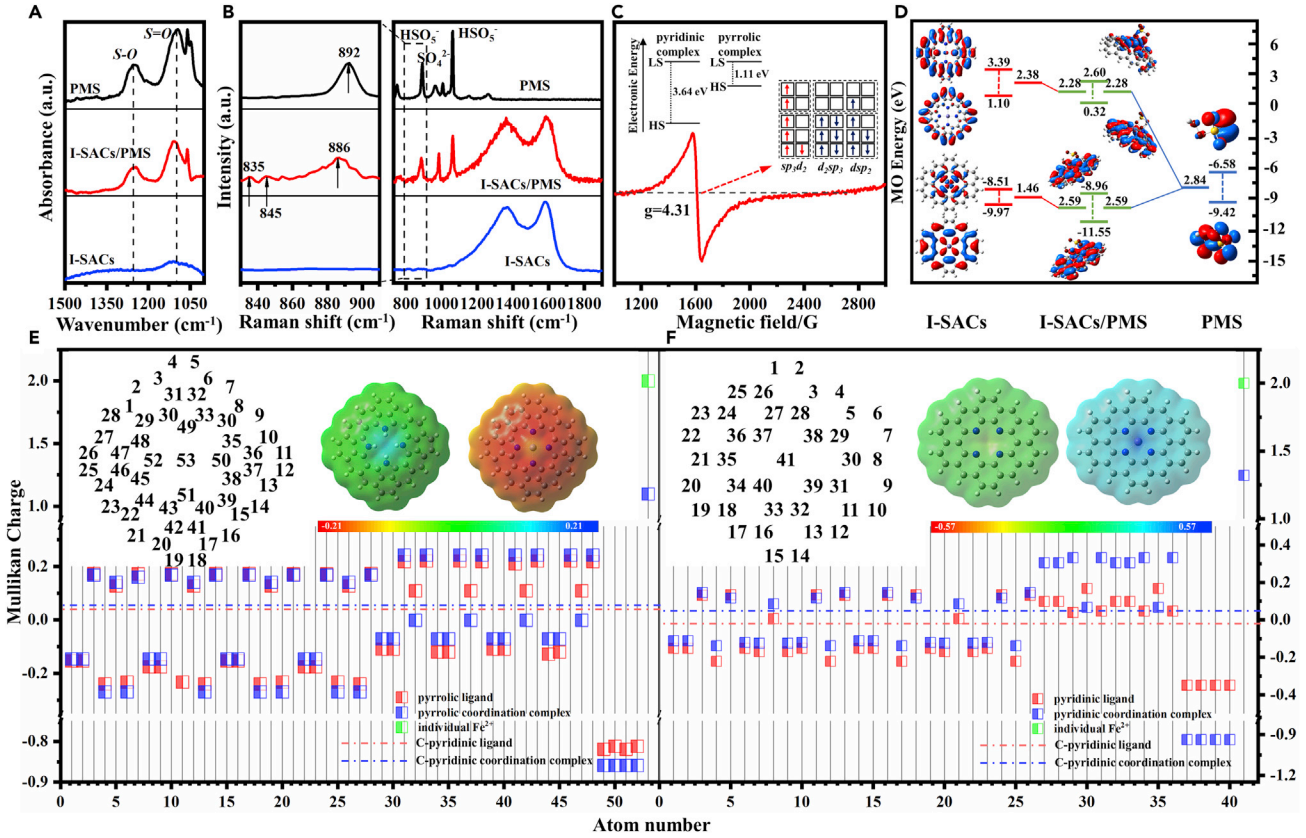

Figure 4. Mechanism investigation

(A) ATR-FT-IR analysis of I-SACs, PMS, and I-SACs/PMS system.

(B) *In situ* Raman analysis of I-SACs, PMS, and I-SACs/PMS process.

(C) Spin state and EPR analysis (at 77 K) of I-SACs.

(D) Molecular orbital energy of pyrrolic-complex/PMS and pyridinic-complex/PMS.

(E) ESP and Mulliken charge population of pyrrolic ligand and corresponding pyrrolic Fe-N coordination complexes.

(F) ESP and Mulliken charge population of pyridinic ligand and corresponding pyrrolic Fe-N coordination complexes.

were not robust catalytic active sites.[48] I-t curves further showed that a strong current (0.171×10^{-5} A) was generated once PMS was added to the solution (Figure 3D), evidencing electron transfer from I-SACs to the surface-adsorbed PMS. In addition, the addition of AAP to the I-SACs/PMS system instantly decreased the current generation to 0.126×10^{-5} A. This phenomenon demonstrated the electron transfer from adsorbed AAP to PMS* to stabilize the surface potential of the I-SACs/PMS* complex, culminating in the simultaneous degradation of AAP. Linear sweep voltammetry analysis obtained the same tendency that the addition of AAP decreased the current density generated by I-SACs/PMS (Figure S5F). Additional confirmation was obtained through *in situ* Raman analysis (Figure 4B). The peak positioned at 892 cm^{-1} in the PMS solution was ascribed to the O-O bond of PMS. When I-SACs was added to the PMS solution, the peak of the O-O bond shown in blue shifted from 892 to 886 cm^{-1}, indicating a change in the vibration model of the O-O bond in PMS. This result also indicates that PMS was successfully adsorbed on the surface of I-SACs. More importantly, a new vibration band emerged in the range of 835 to 845 cm^{-1}. The newly appeared vibration band was absent in both the individual PMS solution and I-SACs groups, which could be assigned to PMS*.[49] Attenuated total reflectance Fourier transform infrared spectroscopy analysis demonstrated the possible cleavage of the S-O bond of PMS when PMS coexisted with I-SACs (Figure 4A), further indicating that the adsorbed PMS was activated. In addition, these results also suggest the possible generation pathway of $^1O_2$ through $O_2^{\cdot-}$ disproportionation reported in the literature[50] (Equation 1). Furthermore, the self-decay of adsorbed PMS might also contribute to the generation of $^1O_2$[51] (Equation 2).

$$2O_2^{\cdot-} \xrightarrow{disproportionation} x^1O_2 + (1-x)^3O_2 + O_2^{2-}\ 0 \le x \le 1 \qquad \text{(Equation 1)}$$

$$SO_5^{2-} + HSO_5^- \rightarrow SO_4^{2-} + HSO_4^- + x^1O_2 + (1 - x)^3O_2\ 0 \leq x \leq 1 \quad \text{(Equation 2)}$$

Finally, the generation of ferryl species ($Fe^{IV} = O^{2+}$) should be considered.[52] $Fe^{IV} = O^{2+}$ is usually generated via a two-electron transfer process with the cleavage of PMS when it reacts with Fe^{2+}.[53] To confirm the involvement of $Fe^{IV} = O^{2+}$ in the I-SACs/PMS process, methyl phenyl sulfoxide (PMSO) was used as a probe because $Fe^{IV} = O^{2+}$ could oxidize PMSO and generate equivalent methyl phenyl sulfone ($PMSO_2$) through an oxygen atom transfer process.[54] As shown in Figure 3E, circa 1.8 μM PMSO was degraded within 5 min. Accordingly, 1.5 μM $PMSO_2$ was generated simultaneously, possibly indicating the involvement of $Fe^{IV} = O^{2+}$ in the I-SACs/PMS process. However, it was found that 1.3 μM of $PMSO_2$ was generated when PMS reacted with PMSO in the absence of I-SACs within 5 min, and more than 9.1 μM of $PMSO_2$ could be generated if the reaction time increased to 1 h. Furthermore, about 9.0 μM $PMSO_2$ was generated within 1 h in the I-SACs/PMS process, which equaled the transformation ratio by the individual PMS solution (Figure 3F). By comparison, when Fe^{2+} was used as an activator, more than 15.8 μM of PMSO was degraded and 14.1 μM of $PMSO_2$ was generated. Based on the above results, it could be concluded that the slightly generated $PMSO_2$ was caused by the reaction between PMS and PMSO, rather than I-SACs. More importantly, the experimental results of PMS/PMSO, Fe^{2+}/PMS/PMSO, and I-SACs/PMS/PMSO system also suggested that the accuracy of the PMSO-$PMSO_2$ method for ferryl species identification in a heterogeneous process should be reconsidered.

Mechanisms of ROS generation and pollutant oxidation

Density functional theory calculation

Theoretical calculations were carried out to determine the mechanism of ROS generation in the I-SACs/PMS process. A Fe-N-C structure was created to mimic the possible atomic cluster of I-SACs by using iron and pyridinic N-doped carbon matrix as a metal center and ligand, respectively, which has been widely used in the literature.[26–28] However, considering the possible coordination between pyrrolic N and iron, such as FePc, an atomic cluster with pyrrolic ligand was also considered. The iron center and ligand should be d^2sp^3, dsp^2, or sp^3d^2 hybridization because the valent electron distribution of ground state Fe^{II} is $[Ar]3d^6$. The possible orbital state is shown in Figure 4C, suggesting singlet, triplet, and quintet spin multiplicity. According to Hund's rule and density functional theory (DFT) calculation, the quintet state possessed the most thermodynamic stability, and the sp^3d^2 hybrid model possessed the lowest formation energy. Low-temperature solid EPR analysis further confirmed the high spin state of the Fe center with a g factor of 4.31 (Figure 4C),[55] corroborated with the Mössbauer analysis.

Electrostatic potential (ESP) analysis shown in Figures 4E and 4F demonstrated the most positive ESP of the iron center, indicating that the iron center might be favorable for PMS adsorption. Moreover, Mulliken charge analysis (Figures 4E and 4F) showed that the maximum electron density was located on the nitrogen sites in the ligand, and the iron center possessed the most positive charge in the cluster. It also could be observed that the average Mulliken charge of all carbon sites in the ligand was more negative than that in the iron-ligand coordination complex with a further decreased charge of the iron center. This observation demonstrated an electron transfer process from the ligand to the metal center.

Frontier molecular orbital theory proposed the importance of the highest occupied molecular orbital (HOMO) and lowest unoccupied molecular orbital (LUMO).[56] The energy gap between HOMO and LUMO ($E_{L\text{-}H}$) usually describes the stability of substances, with smaller $E_{L\text{-}H}$ always causing higher chemical reactivity. Considering the high spin state of the current system, the chemical reactivity was explored by using the singly occupied molecular orbital (SOMO, E_S). For a pyrrolic-type coordination complex, the $E_{L\text{-}S(4)}$ (energy gap between $SOMO_4$ and LUMO) of the individual PMS and the complex was 2.84 and 2.38 eV, respectively. After PMS adsorption on the surface of the complex, $E_{L\text{-}S(4)}$ decreased to 2.28 eV, indicating the reactivity of PMS adsorbed on the iron center of the complex was considerably increased (Figure 4D). For a pyridinic-type coordination complex, the $E_{L\text{-}S(4)}$ of PMS decreased to 2.59 eV when it was adsorbed on the surface of the complex. The lower $E_{L\text{-}S(4)}$ of the coordination complex/PMS than individual PMS demonstrated that I-SACs with both pyrrolic and pyridinic ligands were all capable of PMS activation. In addition, the higher $SOMO_4$ energy of the pyrrolic-type I-SACs also suggested stronger chemical reactivity than pyridinic-type I-SACs. Notably, the valent of the iron center would be increased ($Fe^{II \rightarrow III}$) after electron donation to PMS for radical generation. However, due to the very low redox potential of Fe^{III}/Fe^{II} (0.8 V), the reduction of Fe^{III} into Fe^{II} is extraordinarily ineffective.[57] For example, Fe^{2+}/PMS only exhibited a significant oxidation performance in the preliminary stage, which is largely different

from that of Co^{2+}/PMS due to the Co^{III}/Co^{II} (1.9 V) redox cycle being spontaneous in the PMS solution (Figure S6A).[58] However, the XPS spectrum after reaction emphasized that the center of Fe $2p_{3/2}$ was still positioned at a low binding energy (711.2 eV), indicating that Fe atoms still exist in a low redox state after reaction (Figure S1H). Meanwhile, Figure S4B demonstrated the catalytic performance of I-SACs in consecutive runs, indicating spontaneous Fe^{III}/Fe^{II} redox cycling during the reaction. By comparison, in the Fe^{3+}/H_2O_2 system, more than 72.3% of Fe^{3+} could be reduced into Fe^{2+} due to the reductive capability of H_2O_2 (Figure S6B). However, the concentration of Fe^{2+} detected in the Fe^{3+}/PMS process was negligible. This observation emphasized that the spontaneous Fe^{III}/Fe^{II} redox cycling in I-SACs was not caused by electron donation from PMS to the active site (Fe^{III}) because PMS is incapable of disproportionation like H_2O_2. Therefore, the mechanism of spontaneous Fe^{III}/Fe^{II} redox cycling is still unclear and should be carefully investigated.

Conjugation and electron delocalization

The short-range-ordered carbon framework always possesses a conjugated electronic structure even with the doping of heteroatom nitrogen. The conjugation effect is also known as the delocalization effect, namely that π electrons in the conjugated electronic structure are free to remove in all C atoms without the limitation of the transfer distance through delocalized π orbitals. More importantly, any substituent with stronger electron attraction performance would decrease the π electrons wave function in the conjugation matrix. Consequently, the electron density in the substituent would be elevated considerably. N possesses a higher electronegativity (3.07) than C (2.50); the delocalized π electrons would be therefore concentrated on the heteroatom N.

Local orbital locator (LOL) analysis demonstrated that the nitrogen sites possessed the highest π electron density in the conjugation structure. Also, pyrrolic-type ligands possessed higher π electron density than pyridinic-type ligands (Figures 5A and 5B), indicating stronger electron delocalization.[59] When iron coordinated with the conjugated N-C matrix, the assembly of delocalized π electrons on the iron center could be observed, suggesting a decreased redox state of the iron center. In addition, DFT calculation also evidenced the high spin state of the iron center (Figures 5C and 5D), corroborating the EPR and Mössbauer spectra. Therefore, it is inferred that the delocalized π electrons facilitated the Fe^{III}/Fe^{II} redox cycling of the iron center through a ligand-to-metal electron transfer. This inference explains the continuous generation of radicals in the I-SACs/PMS process. In addition, the density of delocalized electrons on the iron center in pyridinic-type I-SACs was largely lower than that of the pyrrolic-type I-SACs, and the spin density in the pyridinic-type I-SACs was also largely dispersed. This observation indicated a stronger performance of the pyrrolic-type ligand on Fe^{III}/Fe^{II} redox cycling than the pyridinic-type ligand. The total density of states and partial density of states shown in Figures 5E and 5F demonstrated several overlapped energy states across the Fermi level, suggesting the effective catalytic performance of the atomic cluster.[60,61] The energy states were all contributed by Fe 3d, C 2p, and N 2p. During the interaction between the adsorbate (PMS) and iron center, delocalized electrons accepted by 3d orbitals of Fe from the ligand are further back-donated to the lowest unoccupied molecular orbital.[62] The adsorbed PMS are therefore activated for the generation of radicals by accepting the electrons. For an in-depth assessment of the synergism between the iron center and ligands for spontaneous Fe^{III}/Fe^{II} redox cycling, the ligand-field theory was employed.

Ligand-field theory-based explanation of spontaneous Fe^{III}/Fe^{II} redox cycling

The ligand-field theory postulates that a high-spin metal center in a coordination complex usually occurs when the metal center is coordinated with weak-field ligands. By contrast, a low-spin metal center usually exists when it is coordinated with strong-field ligands. The coordination complexes created by the metal and weak-field ligands would cause a high energy e_g* (antibonding) orbital and a low energy t_{2g}* (antibonding) orbital, culminating in better electron transfer from ligand to metal. However, coordination complexes created by the metal and strong-field ligands would cause a low energy e_g* orbital and high t_{2g}* orbital, resulting in a possible electron transfer from metal to ligand, and therefore inhibiting its electron donation performance. Considering the high-spin-dominated metal species in I-SACs, it could be deemed and discussed as a coordination complex that is created by iron and weak-field ligands.

The formation of the weak ligand fields is shown in Figures 5G and 5H. The interaction between the π-orbital of the ligand and the 3d (t_{2g}) orbital of Fe^{II} formed two new molecular orbitals of the complex, including a bonding orbital (t_{2g}) with low energy and an antibonding orbital (t_{2g}*) with high energy. Since

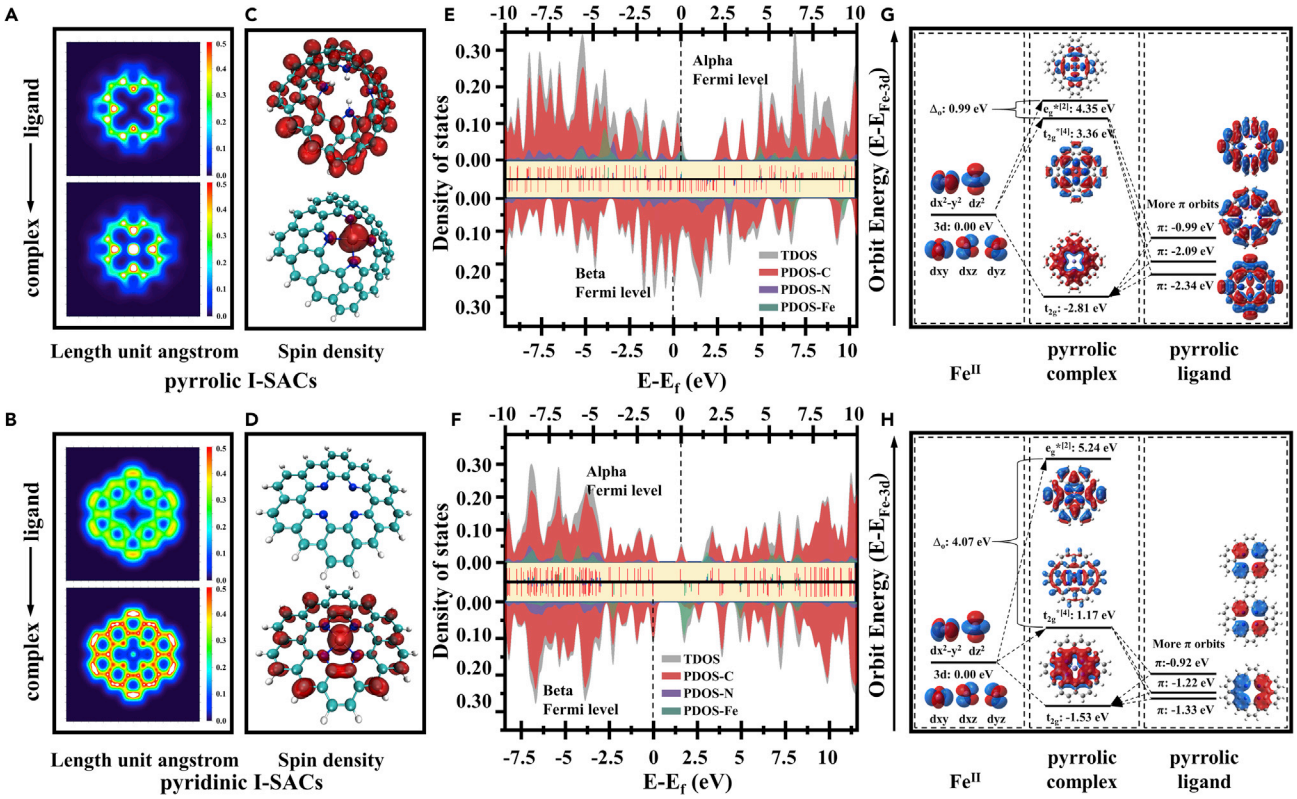

Figure 5. Electronic structure analysis of pyrrolic- and pyridinic-ligand and corresponding I-SACs

(A) Localized orbital locator (LOL) analysis of π electrons in the pyrrolic I-SACs.

(B) LOL analysis of π electrons in the pyridinic I-SAC.

(C) Electron spin density (ESD) of the pyrrolic I-SAC.

(D) ESD of the pyridinic I-SAC.

(E) Total density-of-states (TDOS) and partial density-of-states (PDOS) of the pyrrolic I-SAC.

(F) TDOS and PDOS of the pyridinic I-SAC.

(G) The formation of ligand-field by Fe^{II} 3d and pyrrolic ligand.

(H) The formation of ligand-field by Fe^{II} 3d and pyridinic ligand.

the π-orbital in the ligand possessed lower energy than the 3d orbital of Fe^{II}, the delocalized π electrons would first occupy the newly formed t_{2g} bonding orbital in the coordination complex. Electrons in d_{xy}, d_{yz}, and d_{xz} of Fe^{II} would then occupy the antibonding orbital (t_{2g}*→t_{2g}*[4]), and electrons in d_{z^2} and $d_{x^2-y^2}$ occupied the e_g* orbital (e_g*→e_g*[2]), giving rise to a weak-field ligand-encircled iron center.

The high spin nature of the complex facilitated a "d-d" ligand field transition from t_{2g}*[4] to e_g*[2].[63] Notably, the gaps between e_g*[2] and t_{2g}*[4] is 0.99 eV in the pyrrolic complex, which is considerably smaller than that of the pyridinic complex (4.07 eV), suggesting a stronger electron donation tendency than the pyridinic complex. Considering the t_{2g} orbital is occupied by delocalized π electrons, the iron center would work as a carrier of electrons, culminating in spontaneous Fe^{III}/Fe^{II} redox cycling and the generation of radicals.

This result substantiates the finding from the XPS analysis. However, it also should be noted that XPS analysis is still inaccurate for the measurement of the redox state of iron due to the comparatively low signal-to-noise ratio. Therefore, to find solid experimental evidence for this theory, two coordination complexes were created in solution by using the same metal center (Fe^{3+}) and similar organic ligands (pyrrole/pyridine monomer to create $[Fe(pyrrole)_n]^{3-n}$ and $[Fe(pyridine)_n]^{3+}$). The PMS activation performance of the complexes was subsequently explored. As shown in Figure 6A, more than 45% of AAP was degraded by $[Fe(pyrrole)_n]^{3-n}$/PMS within 30 min. Furthermore, oxidation performance was observed to gradually decrease, suggesting that the conjugation structure of the ligand was destroyed or attenuated due to the continuous electron donation to the iron center. Nonetheless, the oxidation performance recovered

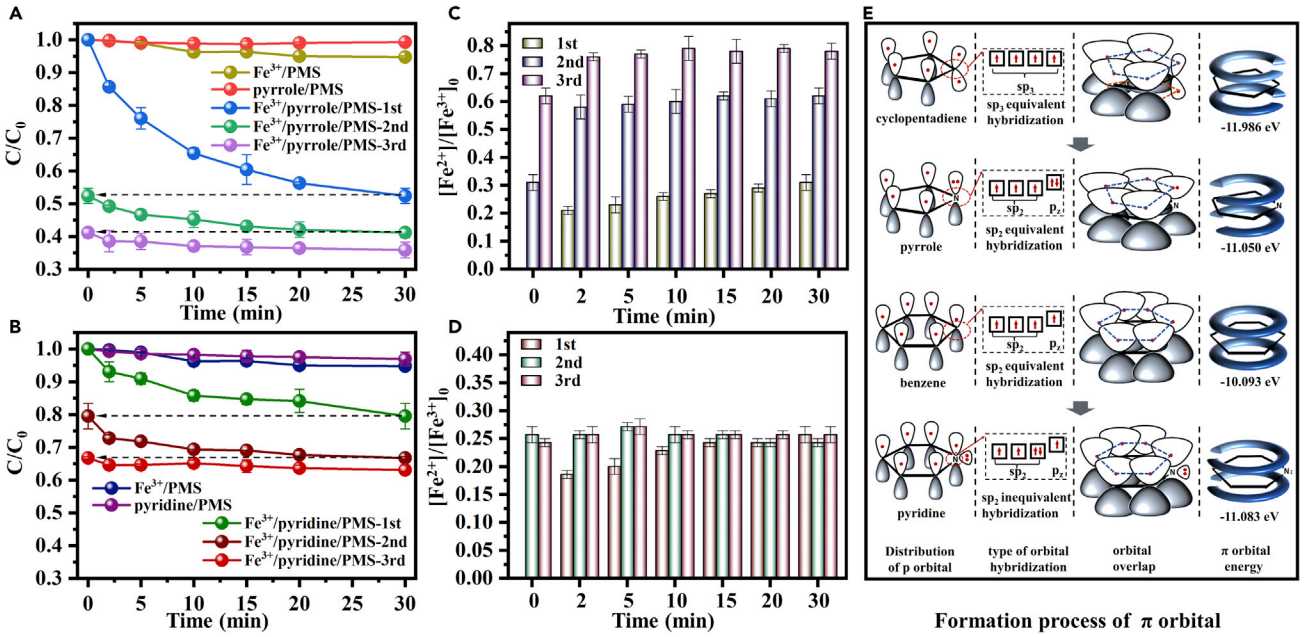

Figure 6. Reactivity investigation between Fe^{3+} and different ligands

(A) AAP degradation by the $[Fe(pyrrole)_n]^{3-n}$/PMS system in consecutive runs ($[Fe^{3+}]$ = 10 μM, [AAP] = 10 μM, [PMS] = 0.5 mM, [pyrrole] = 0.5 mM, [pH] = 2.0 ± 0.1, [Temperature] = 25 ± 0.3°C).

(B) AAP degradation by the $[Fe(pyridine)_n]^{3-n}$/PMS system in consecutive runs ($[Fe^{3+}]$ = 10 μM, [AAP] = 10 μM, [PMS] = 0.5 mM, [pyridine] = 0.5 mM, [pH] = 2.0 ± 0.1, [Temperature] = 25 ± 0.3°C).

(C) Reduction of Fe^{3+} into Fe^{2+} in the $[Fe(pyrrole)_n]^{3-n}$/PMS system in consecutive runs ($[Fe^{3+}]$ = 10 μM, [AAP] = 10 μM, [PMS] = 0.5 mM, [pyrrole] = 0.5 mM, [pH] = 2.0 ± 0.1, [Temperature] = 25 ± 0.3°C).

(D) Reduction of Fe^{3+} into Fe^{2+} in the $[Fe(pyridine)_n]^{3-n}$/PMS system in consecutive runs ($[Fe^{3+}]$ = 10 μM, [AAP] = 10 μM, [PMS] = 0.5 mM, [pyridine] = 0.5 mM, [pH] = 2.0 ± 0.1, [Temperature] = 25 ± 0.3°C).

(E) The evolution of delocalized π orbitals of pyrrole, pyridine, and their isoelectronic species (cyclopentadiene→pyrrole, benzene→pyridine).

with the continuous addition of pyrrole, which can be attributed to the recharge of active ligands to facilitate the Fe^{3+}/Fe^{2+} redox cycling. Similar results were obtained with $[Fe(pyridine)_n]^{3+}$/PMS, whereby about 20% of AAP could be degraded within 30 min, and the oxidation performance was well recovered after the addition of pyridine when the oxidation performance started to attenuate (Figure 6B). In addition, the dynamic transformation of Fe^{3+} into Fe^{2+} was evaluated simultaneously. Circa 21% of Fe^{3+} was reduced into Fe^{2+} once pyrrole was added to the Fe^{3+} solution, which gradually increased to 31% after 30 min (Figure 6C). Further addition of pyrrole significantly facilitated Fe^{3+} reduction that more than 62% of Fe^{3+} was reduced into Fe^{2+} in the second round, and 78% of Fe^{3+} was reduced into Fe^{2+} in the third round. Similarly, about 18% of Fe^{3+} was reduced into Fe^{2+} once pyridine was added to the solution and increased to 25% (Figure 6D). This observation underlined an important conclusion that it was difficult for the iron center to maintain a long-term radical generation performance due to the attenuation of delocalized π orbitals in the ligands. I-SACs possessed a similar electronic structure to the complex discussed above, and therefore the catalytic performance of I-SACs in the radical pathway could not be maintained for a long time as well (the non-radical pathway might not be seriously influenced due to the different mechanism). In addition, the comparatively low Fe^{2+} generation and PMS activation performance of $[Fe(pyridine)_n]^{3+}$ also supports the previous discussion of the ligand field.

Finally, the conjugation states of pyrrolic and pyridinic ligands were investigated (Figure 6E) by using a pyrrole/pyridine monomer and corresponding isoelectronic species (cyclopentadiene for pyrrole and benzene for pyridine). Cyclopentadiene was shown to exhibit a weaker delocalized π orbital (−11.99 eV) than benzene (−10.09 eV) because the C1 in cyclopentadiene is an sp^3 equivalent hybridization and all the C atom in benzene are sp^2 equivalent hybridization. When N substituted C1 sites to form pyrrole and pyridine from cyclopentadiene and benzene, respectively, the hybridization of the N1 site in pyrrole was transformed into an sp^2 equivalent hybridization, resulting in an extension of the delocalized π orbital

and elevated orbital energy (−11.05 eV). On the contrary, the delocalized π orbital was limited with decreased energy of −11.08 eV in pyridine and, so, C4 escaped from the conjugation simultaneously when compared with benzene. This phenomenon was caused by inequivalent sp^2 hybridization of N1 that two lone-pair electrons were populated locally, which could not participate in the conjugation. The lone-pair electrons would exhibit a strong shielding effect (electrostatic repulsion), causing inhibition in the synergism between the Fe center and delocalized π orbital to N1 sites.[64] Similar shielding and repulsion are absent in pyrrole. Therefore, the spontaneous Fe^{3+}/Fe^{2+} redox cycle would be inhibited to a certain extent when iron coordinated with pyridine, further explaining the lower catalytic performance of $[Fe(pyridine)_n]^{3+}$ than $[Fe(pyrrole)_n]^{3-n}$. In addition, it also could be inferred that pyridinic compounds possessed stronger coordination performance with iron than pyrrolic compounds, according to the ligand-field theory. Therefore, the possible pyrrolic ligands might be favorable in elevating the catalytic performance of I-SACs, which should be considered in future studies.

Conclusions

Iron-centered single-atom catalyst (I-SACs) usually exhibits impressive PMS activation performance for organic pollutant degradation. The widely generated $SO_4^{\cdot-}$ and HO• in I-SACs/PMS process are still lacking investigation to explain the facilitated Fe^{III}/Fe^{II} redox cycle in I-SACs. This study demonstrated that the spontaneous Fe^{III}/Fe^{II} redox cycle in I-SACs could be well explained by the ligand-field theory. The nitrogen-containing carbon framework coordinated with iron to create a weak-ligand field, culminating in a ligand-to-metal electron transfer due to the delocalized π orbital in the ligands. Consequently, the high spin iron center could be maintained in a low redox state, further facilitating PMS activation for the generation of $SO_4^{\cdot-}$/HO•. The pyrrolic ligand proved to be highly favorable for PMS activation than the pyridinic ligand due to its weaker coordination performance with iron, which is very important for the design and synthesis of single-atom catalysts in the future. Overall, the results of this study considerably advance our understanding of the mechanism of PMS activation by iron-centered single-atom catalysts. The roles of the conjugation effect and the delocalization of electrons in the ligands of SACs should be the focus of further research for better evolution of advanced oxidation processes.

Limitations of the study

Fe^{III}/Fe^{II} redox cycling in I-SACs was proved to be spontaneous due to the ligand-field effect, which is responsible for the generation of sulfate and hydroxyl radicals when I-SACs was used as a catalyst for peroxymonosulfate activation. Effective degradation of organic pollutants always required a significant generation of radicals. Therefore, the long-time Fe^{III}/Fe^{II} redox cycling in I-SACs was favorable during the degradation process. However, the electronic structure attenuation of the ligand during the reaction is inevitable due to the continuous electron donation from the ligand to the metal center, suggesting a primary difficulty in self-sustaining the spontaneous Fe^{III}/Fe^{II} redox cycling without external energy. The degradation of organic pollutants would be limited by the attenuation of the ligand-field effect. Therefore, I-SACs coupling with external energy might be a promising method for the effective degradation of organic pollutants, and the role of the ligand-field effect in the presence of external energy requires further investigation.

STAR★METHODS

Detailed methods are provided in the online version of this paper and include the following:

- KEY RESOURCES TABLE
- RESOURCE AVAILABILITY
  - Lead contact
  - Materials availability
  - Data and code availability
- METHOD DETAILS
  - Preparation of catalysts
  - Characterization of catalysts
  - Degradation of pollutions
  - Electrochemical measurements
  - Computations
- QUANTIFICATION AND STATISTICAL ANALYSIS
- ADDITIONAL RESOURCES

SUPPLEMENTAL INFORMATION

Supplemental information can be found online at https://doi.org/10.1016/j.isci.2022.105902.

ACKNOWLEDGMENTS

This work was supported by the new style think tank of Shaanxi Universities (20JT041) and the Yanta scholar project of XAUAT.

AUTHOR CONTRIBUTIONS

Conceptualization, S.Y., R.C., and D.D.; methodology, L.W., Y.T., and Z.Q.; investigation, S.Y.; writing – original draft, Z.Q. and S.Y.; writing – review & editing, Z.Q., S.Y., G.W., R.C., and M.D.; supervision, S.Y. and R.C.

DECLARATION OF INTERESTS

The authors declare no competing interests.

Received: September 26, 2022
Revised: November 21, 2022
Accepted: December 21, 2022
Published: January 20, 2023

REFERENCES

1. Qiao, M., Wu, X., Zhao, S., Djellabi, R., and Zhao, X. (2020). Peroxymonosulfate enhanced photocatalytic decomposition of silver-cyanide complexes using g-C3N4 nanosheets with simultaneous recovery of silver. Appl. Catal. B Environ. *265*, 118587. https://doi.org/10.1016/j.apcatb.2020.118587.

2. Zhu, G., Li, X., Wang, H., and Zhang, L. (2017). Microwave assisted synthesis of reduced graphene oxide incorporated MOF-derived ZnO composites for photocatalytic application. Catal. Commun. *88*, 5–8. https://doi.org/10.1016/j.catcom.2016.09.024.

3. Hong, Z., Zhen, Y., Ruan, Y., Kang, M., Zhou, K., Zhang, J.-M., Huang, Z., and Wei, M. (2018). Rational design and general synthesis of S-doped hard carbon with tunable doping sites toward excellent Na-ion storage performance. Adv. Mater. *30*, 1802035. https://doi.org/10.1002/adma.201802035.

4. Ming, H., Zhang, P., Yang, Y., Zou, Y., Yang, C., Hou, Y., Ding, K., Zhang, J., and Wang, X. (2022). Tailored poly-heptazine units in carbon nitride for activating peroxymonosulfate to degrade organic contaminants with visible light. Appl. Catal. B Environ. *311*, 121341. https://doi.org/10.1016/j.apcatb.2022.121341.

5. He, Y.-L., He, C.-S., Lai, L.-D., Zhou, P., Zhang, H., Li, L.-L., Xiong, Z.-K., Mu, Y., Pan, Z.-C., Yao, G., and Lai, B. (2022). Activating peroxymonosulfate by N and O Co-doped porous carbon for efficient BPA degradation: a Re-visit to the removal mechanism and the effects of surface unpaired electrons. Appl. Catal. B Environ. *314*, 121390. https://doi.org/10.1016/j.apcatb.2022.121390.

6. Zhang, X., Feng, M., Wang, L., Qu, R., and Wang, Z. (2017). Catalytic degradation of 2-phenylbenzimidazole-5-sulfonic acid by peroxymonosulfate activated with nitrogen and sulfur co-doped CNTs-COOH loaded CuFe2O4. Chem. Eng. J. *307*, 95–104. https://doi.org/10.1016/j.cej.2016.08.078.

7. Pan, X., Chen, J., Wu, N., Qi, Y., Xu, X., Ge, J., Wang, X., Li, C., Qu, R., Sharma, V.K., and Wang, Z. (2018). Degradation of aqueous 2, 4, 4′-Trihydroxybenzophenone by persulfate activated with nitrogen doped carbonaceous materials and the formation of dimer products. Water Res. *143*, 176–187. https://doi.org/10.1016/j.watres.2018.06.038.

8. Su, Y., Lu, M., Su, R., Zhou, W., Xu, X., and Li, Q. (2022). A 3D MIL-101@rGO composite as catalyst for efficient conversion of straw cellulose into valuable organic acid. Chin. Chem. Lett. *33*, 2573–2578. https://doi.org/10.1016/j.cclet.2021.08.078.

9. Wang, G., Chen, S., Quan, X., Yu, H., and Zhang, Y. (2017). Enhanced activation of peroxymonosulfate by nitrogen doped porous carbon for effective removal of organic pollutants. Carbon *115*, 730–739. https://doi.org/10.1016/j.carbon.2017.01.060.

10. Singh, B., Gawande, M.B., Kute, A.D., Varma, R.S., Fornasiero, P., McNeice, P., Jagadeesh, R.V., Beller, M., and Zbořil, R. (2021). Single-atom (Iron-Based) catalysts: synthesis and applications. Chem. Rev. *121*, 13620–13697. https://doi.org/10.1021/acs.chemrev.1c00158.

11. Singh, B., Sharma, V., Gaikwad, R.P., Fornasiero, P., Zbořil, R., and Gawande, M.B. (2021). Single-atom catalysts: a sustainable pathway for the advanced catalytic applications. Small *17*, 2006473. https://doi.org/10.1002/smll.202006473.

12. Lu, G., Sun, K., Lin, Y., Du, Q., Zhang, J., Wang, K., and Wang, P. (2022). Single-atomic-site iron on N-doped carbon for chemoselective reduction of nitroarenes. Nano Res. *15*, 603–611. https://doi.org/10.1007/s12274-021-3526-5.

13. Lu, G.-P., Shan, H., Lin, Y., Zhang, K., Zhou, B., Zhong, Q., and Wang, P. (2021). A Fe single atom on N, S-doped carbon catalyst for performing N-alkylation of aromatic amines under solvent-free conditions. J. Mater. Chem. *9*, 25128–25135. https://doi.org/10.1039/D1TA07673F.

14. Lin, Y., Wang, F., Yu, J., Zhang, X., and Lu, G.-P. (2022). Iron single-atom anchored N-doped carbon as a 'laccase-like' nanozyme for the degradation and detection of phenolic pollutants and adrenaline. J. Hazard Mater. *425*, 127763. https://doi.org/10.1016/j.jhazmat.2021.127763.

15. Sun, K., Shan, H., Neumann, H., Lu, G.-P., and Beller, M. (2022). Efficient iron single-atom catalysts for selective ammoxidation of alcohols to nitriles. Nat. Commun. *13*, 1848. https://doi.org/10.1038/s41467-022-29074-1.

16. Shang, Y., Duan, X., Wang, S., Yue, Q., Gao, B., and Xu, X. (2022). Carbon-based single atom catalyst: synthesis, characterization, DFT calculations. Chin. Chem. Lett. *33*, 663–673. https://doi.org/10.1016/j.cclet.2021.07.050.

17. Yang, M., Hou, Z., Zhang, X., Gao, B., Li, Y., Shang, Y., Yue, Q., Duan, X., and Xu, X. (2022). Unveiling the origins of selective oxidation in single-atom catalysis via Co–N4–C intensified radical and nonradical pathways. Environ. Sci. Technol. *56*, 11635–11645. https://doi.org/10.1021/acs.est.2c01261.

18. Yang, S., Xu, S., Tong, J., Ding, D., Wang, G., Chen, R., Jin, P., and Wang, X.C. (2021). Overlooked role of nitrogen dopant in carbon catalysts for peroxymonosulfate activation: intrinsic defects or extrinsic defects? Appl. Catal. B Environ. *295*, 120291.

https://doi.org/10.1016/j.apcatb.2021.120291.

19. Xu, H., Jiang, N., Wang, D., Wang, L., Song, Y., Chen, Z., Ma, J., and Zhang, T. (2020). Improving PMS oxidation of organic pollutants by single cobalt atom catalyst through hybrid radical and non-radical pathways. Appl. Catal. B Environ. *263*, 118350. https://doi.org/10.1016/j.apcatb.2019.118350.

20. Peng, L., Duan, X., Shang, Y., Gao, B., and Xu, X. (2021). Engineered carbon supported single iron atom sites and iron clusters from Fe-rich Enteromorpha for Fenton-like reactions via nonradical pathways. Appl. Catal. B Environ. *287*, 119963. https://doi.org/10.1016/j.apcatb.2021.119963.

21. Yoo, H.Y., Kim, M.S., Shin, H., and Lim, J. (2022). Peroxymonosulfate activation by black TiO2 nanotube arrays under solar light: switching the activation mechanism and enhancing catalytic activity and stability. J. Hazard Mater. *433*, 128796. https://doi.org/10.1016/j.jhazmat.2022.128796.

22. Bao, Y., Oh, W.-D., Lim, T.-T., Wang, R., Webster, R.D., and Hu, X. (2019). Elucidation of stoichiometric efficiency, radical generation and transformation pathway during catalytic oxidation of sulfamethoxazole via peroxymonosulfate activation. Water Res. *151*, 64–74. https://doi.org/10.1016/j.watres.2018.12.007.

23. Liu, C., Liu, Y., Dang, Z., Zeng, S., and Li, C. (2021). Enhancement of heterogeneous photo-Fenton performance of core-shell structured boron-doped reduced graphene oxide wrapped magnetical Fe3O4 nanoparticles: Fe(II)/Fe(III) redox and mechanism. Appl. Surf. Sci. *544*, 148886. https://doi.org/10.1016/j.apsusc.2020.148886.

24. Lin, J., Zou, J., Cai, H., Huang, Y., Li, J., Xiao, J., Yuan, B., and Ma, J. (2021). Hydroxylamine enhanced Fe(II)-activated peracetic acid process for diclofenac degradation: efficiency, mechanism and effects of various parameters. Water Res. *207*, 117796. https://doi.org/10.1016/j.watres.2021.117796.

25. Wang, J., Li, B., Li, Y., Fan, X., Zhang, F., Zhang, G., and Peng, W. (2021). Facile synthesis of atomic Fe-N-C materials and dual roles investigation of Fe-N4 sites in fenton-like reactions. Adv. Sci. *8*, 2101824. https://doi.org/10.1002/advs.202101824.

26. Chen, G., An, Y., Liu, S., Sun, F., Qi, H., Wu, H., He, Y., Liu, P., Shi, R., Zhang, J., et al. (2022). Highly accessible and dense surface single metal FeN4 active sites for promoting the oxygen reduction reaction. Energy Environ. Sci. *15*, 2619–2628. https://doi.org/10.1039/D2EE00542E.

27. Liu, M., Lee, J., Yang, T.-C., Zheng, F., Zhao, J., Yang, C.-M., and Lee, L.Y.S. (2021). Synergies of Fe single atoms and clusters on N-doped carbon electrocatalyst for pH-universal oxygen reduction. Small Methods *5*, 2001165. https://doi.org/10.1002/smtd.202001165.

28. Chen, G., Liu, P., Liao, Z., Sun, F., He, Y., Zhong, H., Zhang, T., Zschech, E., Chen, M., Wu, G., et al. (2020). Zinc-mediated template synthesis of Fe-N-C electrocatalysts with densely accessible Fe-Nx active sites for efficient oxygen reduction. Adv. Mater. *32*, 1907399. https://doi.org/10.1002/adma.201907399.

29. Zhang, Z., Sun, J., Wang, F., and Dai, L. (2018). Efficient oxygen reduction reaction (ORR) catalysts based on single iron atoms dispersed on a hierarchically structured porous carbon framework. Angew. Chem. Int. Ed. Engl. *57*, 9038–9043. https://doi.org/10.1002/anie.201804958.

30. Lin, L., Zhu, Q., and Xu, A.-W. (2014). Noble-metal-free Fe–N/C catalyst for highly efficient oxygen reduction reaction under both alkaline and acidic conditions. J. Am. Chem. Soc. *136*, 11027–11033. https://doi.org/10.1021/ja504696r.

31. Yang, Z.K., Lin, L., and Xu, A.-W. (2016). 2D Nanoporous Fe−N/C nanosheets as highly efficient non-platinum electrocatalysts for oxygen reduction reaction in Zn-air battery. Small *12*, 5710–5719. https://doi.org/10.1002/smll.201601887.

32. Wang, Y., Cui, X., Zhang, J., Qiao, J., Huang, H., Shi, J., and Wang, G. (2022). Advances of atomically dispersed catalysts from single-atom to clusters in energy storage and conversion applications. Prog. Mater. Sci. *128*, 100964. https://doi.org/10.1016/j.pmatsci.2022.100964.

33. Long, X., Li, Z., Gao, G., Sun, P., Wang, J., Zhang, B., Zhong, J., Jiang, Z., and Li, F. (2020). Graphitic phosphorus coordinated single Fe atoms for hydrogenative transformations. Nat. Commun. *11*, 4074. https://doi.org/10.1038/s41467-020-17903-0.

34. Lin, Y., Liu, K., Chen, K., Xu, Y., Li, H., Hu, J., Lu, Y.-R., Chan, T.-S., Qiu, X., Fu, J., and Liu, M. (2021). Tuning charge distribution of FeN4 via external N for enhanced oxygen reduction reaction. ACS Catal. *11*, 6304–6315. https://doi.org/10.1021/acscatal.0c04966.

35. Ribeiro-Soares, J., Oliveros, M.E., Garin, C., David, M.V., Martins, L.G.P., Almeida, C.A., Martins-Ferreira, E.H., Takai, K., Enoki, T., Magalhães-Paniago, R., et al. (2015). Structural analysis of polycrystalline graphene systems by Raman spectroscopy. Carbon *95*, 646–652. https://doi.org/10.1016/j.carbon.2015.08.020.

36. Jiang, H.-L., Liu, B., Lan, Y.-Q., Kuratani, K., Akita, T., Shioyama, H., Zong, F., and Xu, Q. (2011). From metal–organic framework to Nanoporous carbon: toward a very high surface area and hydrogen uptake. J. Am. Chem. Soc. *133*, 11854–11857. https://doi.org/10.1021/ja203184k.

37. Funke, H., Chukalina, M., and Rossberg, A. (2005). Wavelet analysis of extended XRay absorption fine structure data. Phys. Scripta *232*, 232. https://doi.org/10.1238/physica.topical.115a00232.

38. Bouwkamp-Wijnoltz, A.L., Visscher, W., van Veen, J.A.R., Boellaard, E., van der Kraan, A.M., and Tang, S.C. (2002). On active-site heterogeneity in pyrolyzed carbon-supported iron porphyrin catalysts for the electrochemical reduction of oxygen: an in situ mössbauer study. J. Phys. Chem. B *106*, 12993–13001. https://doi.org/10.1021/jp0266087.

39. Koslowski, U.I., Abs-Wurmbach, I., Fiechter, S., and Bogdanoff, P. (2008). Nature of the catalytic centers of porphyrin-based electrocatalysts for the ORR: a correlation of kinetic current density with the site density of Fe−N4 centers. J. Phys. Chem. C *112*, 15356–15366. https://doi.org/10.1021/jp802456e.

40. Andres, H., Bominaar, E.L., Smith, J.M., Eckert, N.A., Holland, P.L., and Münck, E. (2002). Planar three-coordinate high-spin FeII complexes with large orbital angular momentum: mössbauer, electron paramagnetic resonance, and electronic structure studies. J. Am. Chem. Soc. *124*, 3012–3025. https://doi.org/10.1021/ja012327l.

41. Chen, Y., Zhang, G., Liu, H., and Qu, J. (2019). Confining free radicals in close vicinity to contaminants enables ultrafast fenton-like processes in the interspacing of MoS2 membranes. Angew. Chem. Int. Ed. Engl. *58*, 8134–8138. https://doi.org/10.1002/anie.201903531.

42. Wang, L., Ding, D., Qian, Z., Dzakpasu, M., Chen, R., Wang, G., and Yang, S. (2022). Intensification of van der Waals interaction for efficient peroxymonosulfate activation and accuracy re-evaluation of quenching experiments for reactive oxidation species identification. Chem. Eng. J. *450*, 138353. https://doi.org/10.1016/j.cej.2022.138353.

43. Li, S., Huang, J., Li, X., and Li, L. (2020). The relation of interface electron transfer and PMS activation by the H-bonding interaction between composite metal and MCM-48 during sulfamethazine ozonation. Chem. Eng. J. *398*, 125529. https://doi.org/10.1016/j.cej.2020.125529.

44. Timmins, G.S., Liu, K.J., Bechara, E.J., Kotake, Y., and Swartz, H.M. (1999). Trapping of free radicals with direct in vivo EPR detection: a comparison of 5, 5-dimethyl-1-pyrroline-N-oxide and 5-diethoxyphosphoryl-5-methyl-1-pyrroline-N-oxide as spin traps for HO and SO4·−. Free Radic. Biol. Med. *27*, 329–333. https://doi.org/10.1016/S0891-5849(99)00049-0.

45. Dong, H., Li, Y., Wang, S., Liu, W., Zhou, G., Xie, Y., and Guan, X. (2020). Both Fe(IV) and radicals are active oxidants in the Fe(II)/Peroxydisulfate process. Environ. Sci. Technol. Lett. *7*, 219–224. https://doi.org/10.1021/acs.estlett.0c00025.

46. Huang, K.Z., and Zhang, H. (2019). Direct electron-transfer-based peroxymonosulfate activation by iron-doped manganese oxide (δ-MnO2) and the development of galvanic oxidation processes (GOPs). Environ. Sci. Technol. *53*, 12610–12620. https://doi.org/10.1021/acs.est.9b03648.

47. Shi, Q., Pu, S., Yang, X., Wang, P., Tang, B., and Lai, B. (2022). Enhanced heterogeneous activation of peroxymonosulfate by boosting internal electron transfer in a bimetallic

Fe3O4-MnO2 nanocomposite. Chin. Chem. Lett. *33*, 2129–2133. https://doi.org/10.1016/j.cclet.2021.07.063.

48. Ao, X., Zhang, W., Li, Z., Li, J.-G., Soule, L., Huang, X., Chiang, W.-H., Chen, H.M., Wang, C., Liu, M., and Zeng, X.C. (2019). Markedly enhanced oxygen reduction activity of single-atom Fe catalysts via integration with Fe Nanoclusters. ACS Nano *13*, 11853–11862. https://doi.org/10.1021/acsnano.9b05913.

49. Ren, W., Nie, G., Zhou, P., Zhang, H., Duan, X., and Wang, S. (2020). The intrinsic nature of persulfate activation and N-doping in carbocatalysis. Environ. Sci. Technol. *54*, 6438–6447. https://doi.org/10.1021/acs.est.0c01161.

50. Mourad, E., Petit, Y.K., Spezia, R., Samojlov, A., Summa, F.F., Prehal, C., Leypold, C., Mahne, N., Slugovc, C., Fontaine, O., et al. (2019). Singlet oxygen from cation driven superoxide disproportionation and consequences for aprotic metal–O2 batteries. Energy Environ. Sci. *12*, 2559–2568. https://doi.org/10.1039/C9EE01453E.

51. Wang, Y., Cao, D., and Zhao, X. (2017). Heterogeneous degradation of refractory pollutants by peroxymonosulfate activated by CoOx-doped ordered mesoporous carbon. Chem. Eng. J. *328*, 1112–1121. https://doi.org/10.1016/j.cej.2017.07.042.

52. Wang, Z., Qiu, W., Pang, S., Gao, Y., Zhou, Y., Cao, Y., and Jiang, J. (2020). Relative contribution of ferryl ion species (Fe(IV)) and sulfate radical formed in nanoscale zero valent iron activated peroxydisulfate and peroxymonosulfate processes. Water Res. *172*, 115504. https://doi.org/10.1016/j.watres.2020.115504.

53. Li, F., England, J., and Que, L. (2010). Near-Stoichiometric conversion of H2O2 to FeIV=O at a Nonheme iron(II) center. Insights into the O−O bond cleavage step. J. Am. Chem. Soc. *132*, 2134–2135. https://doi.org/10.1021/ja9101908.

54. Huang, Z.-S., Wang, L., Liu, Y.-L., Zhang, H.-Y., Zhao, X.-N., Bai, Y., and Ma, J. (2021). Ferrate self-decomposition in water is also a self-activation process: role of Fe(V) species and enhancement with Fe(III) in methyl phenyl sulfoxide oxidation by excess ferrate. Water Res. *197*, 117094. https://doi.org/10.1016/j.watres.2021.117094.

55. Arnett, C.H., Oyala, P.H., and Agapie, T. (2021). Probing redox non-innocence in iron–carbene complexes {Fe=C(H)Ar}10–11 by 1, 2H and 13C pulse electron paramagnetic resonance. Angew. Chem. Int. Ed. Engl. *60*, 27220–27224. https://doi.org/10.1002/anie.202110704.

56. Chen, D., and Wang, H. (2019). HOMO–LUMO gaps of homogeneous polycyclic aromatic hydrocarbon clusters. J. Phys. Chem. C *123*, 27785–27793. https://doi.org/10.1021/acs.jpcc.9b08300.

57. Qi, C., Wen, Y., Zhao, Y., Dai, Y., Li, Y., Xu, C., Yang, S., and He, H. (2022). Enhanced degradation of organic contaminants by Fe(III)/peroxymonosulfate process with l-cysteine. Chin. Chem. Lett. *33*, 2125–2128. https://doi.org/10.1016/j.cclet.2021.10.087.

58. Anipsitakis, G.P., and Dionysiou, D.D. (2004). Radical generation by the interaction of transition metals with common oxidants. Environ. Sci. Technol. *38*, 3705–3712. https://doi.org/10.1021/es035121o.

59. van Ree, R., van Leeuwen, W.A., van den Berg, M., Weller, H.H., and Aalberse, R.C. (1994). IgE and IgG cross-reactivity among Lol p I and Lol p II/III. Allergy *49*, 254–261. https://doi.org/10.1111/j.1398-9995.1994.tb02658.x.

60. Zhang, J., Zhao, Y., Chen, C., Huang, Y.-C., Dong, C.-L., Chen, C.-J., Liu, R.-S., Wang, C., Yan, K., Li, Y., and Wang, G. (2019). Tuning the coordination environment in single-atom catalysts to achieve highly efficient oxygen reduction reactions. J. Am. Chem. Soc. *141*, 20118–20126. https://doi.org/10.1021/jacs.9b09352.

61. Liu, Z., Lu, T., and Chen, Q. (2020). An sp-hybridized all-carboatomic ring, cyclo[18] carbon: electronic structure, electronic spectrum, and optical nonlinearity. Carbon *165*, 461–467. https://doi.org/10.1016/j.carbon.2020.05.023.

62. Yang, Y., Li, J., Zhang, C., Yang, Z., Sun, P., Liu, S., and Cao, Q. (2022). Theoretical insights into nitrogen-doped graphene-supported Fe, Co, and Ni as single-atom catalysts for CO2 reduction reaction. J. Phys. Chem. C *126*, 4338–4346. https://doi.org/10.1021/acs.jpcc.1c09740.

63. Yang, Y., Ratner, M.A., and Schatz, G.C. (2014). Multireference Ab initio study of ligand field d–d transitions in octahedral transition-metal oxide clusters. J. Phys. Chem. C *118*, 29196–29208. https://doi.org/10.1021/jp5052672.

64. Kong, X.-P., Shen, X., Jang, J., and Gao, X. (2018). Electron pair repulsion responsible for the peculiar edge effects and surface chemistry of black phosphorus. J. Phys. Chem. Lett. *9*, 947–953. https://doi.org/10.1021/acs.jpclett.8b00128.

65. Miao, J., Geng, W., Alvarez, P.J.J., and Long, M. (2020). 2D N-doped porous carbon derived from polydopamine-coated graphitic carbon nitride for efficient nonradical activation of peroxymonosulfate. Environ. Sci. Technol. *54*, 8473–8481. https://doi.org/10.1021/acs.est.0c03207.

66. Frisch, M. J.; Trucks, G. W.; Schlegel, H. B.; Scuseria, G. E.; Robb, M. A.; Cheeseman, J. R.; Scalmani, G.; Barone, V.; Petersson, G. A.; Nakatsuji, H.; et al. Gaussian 16., Revision C.01.01. Gaussian, Inc., Wallingford CT (2016).

67. Grimme, S., Antony, J., Ehrlich, S., and Krieg, H. (2010). A consistent and accurate ab initio parametrization of density functional dispersion correction (DFT-D) for the 94 elements H-Pu. J. Chem. Phys. *132*, 154104. https://doi.org/10.1063/1.3382344.

68. Lu, T., and Chen, F. (2012). Multiwfn: a multifunctional wavefunction analyzer. J. Comput. Chem. *33*, 580–592.

69. Lu, T., and Chen, Q. (2020). A simple method of identifyingπ orbitals for non-planar systems, and a protocol of studyingπ electronic structure. Theor. Chem. Acc. *139*, 25. https://doi.org/10.1007/s00214-019-2541-z.

STAR★METHODS

KEY RESOURCES TABLE

REAGENT or RESOURCE	SOURCE	IDENTIFIER
Chemicals, peptides, and recombinant proteins		
Nafion 117 solution	Shanghai Aladdin Bio-Chem Technology Co., LTD	CAS:31175-20-9
Bisphenol A (BPA)	Shanghai Aladdin Bio-Chem Technology Co., LTD	CAS:80-05-7
Sodium sulfate anhydrous (Na2SO4)	Shanghai Aladdin Bio-Chem Technology Co., LTD	CAS:7757-82-6
Pyrrole	Shanghai Macklin Biochemical Technology Co., LTD	CAS:109-97-7
Iron (II) Acetate tetrahydrate	Shanghai Macklin Biochemical Technology Co., LTD	CAS:3094-87-9
4-Acetamidophenol (AAP)	Shanghai Macklin Biochemical Technology Co., LTD	CAS:103-90-2
2,4,6-Trichlorophenol (2,4,6-TCP)	Shanghai Macklin Biochemical Technology Co., LTD	CAS:88-06-2
Phenol	Shanghai Macklin Biochemical Technology Co., LTD	CAS:108-95-2
Sulfamethoxazole (SMX)	Shanghai Macklin Biochemical Technology Co., LTD	CAS:723-46-6
Ibuprofen (IBU)	Shanghai Macklin Biochemical Technology Co., LTD	CAS:15687-27-1
Carbamazepine (CBZ)	Shanghai Macklin Biochemical Technology Co., LTD	CAS:298-46-4
Potassium monopersulfate triple salt (PMS)	Shanghai Macklin Biochemical Technology Co., LTD	CAS:70693-62-8
2,2,4,6-Tetramethyl-4-piperidinol (TEMP)	Shanghai Macklin Biochemical Technology Co., LTD	CAS:2403-88-5
5,5-Dimethyl-1-pyrroline N-oxide (DMPO)	Shanghai Macklin Biochemical Technology Co., LTD	CAS:3317-61-1
Methyl phenyl sulfoxide (PMSO)	Shanghai Macklin Biochemical Technology Co., LTD	CAS:1193-82-4
Methyl phenyl sulfone ($PMSO_2$)	Shanghai Macklin Biochemical Technology Co., LTD	CAS:3112-85-4
1,10-Phenanthroline	Tianjin Kemiou Chemiical Reagent Co., LTD	CAS:66-71-7
Sodium hydroxide (NaOH)	Tianjin Kemiou Chemiical Reagent Co., LTD	CAS:1310-73-2
Acetic acid	Tianjin Kemiou Chemiical Reagent Co., LTD	CAS:64-19-7
Potassium bromide (KBr)	Tianjin Kemiou Chemiical Reagent Co., LTD	CAS:7758-02-3
Dimethyl sulfoxide (DMSO)	Tianjin Kemiou Chemiical Reagent Co., LTD	CAS:67-85
Absolute alcohol	Tianli Chemical Reagent Co., LTD	CAS:64-17-5
Tert-Butyl alcohol (TBA)	Tianli Chemical Reagent Co., LTD	CAS:75-65-0

(*Continued on next page*)

Continued

REAGENT or RESOURCE	SOURCE	IDENTIFIER
Benzoic acid (BA)	Tianli Chemical Reagent Co., LTD	CAS:65-85-0
p-Hydroxybenzoic acid (p-HBA)	Tianli Chemical Reagent Co., LTD	CAS:99-96-7
Nitric (HNO_3)	Guangdong Guanghua Sci-Tech Co., LTD	CAS:7697-37-2
L-histidine (L-his)	Shanghai Lanji technology development Co., LTD	CAS:71-00-1
Methanol (Meth)	Thermo Fisher Scientific	CAS:67-56-1
Acetonitrile	Thermo Fisher Scientific	CAS:75-05-8
Software and algorithms		
OriginPro 2018	Origin Lab	https://originlab.com
Power point	Microsoft 365	https://microsoft.com
Word	Microsoft 365	https://microsoft.com
Gaussian 16 W.1B	Gaussian, inc.	https://gaussian.com
GaussView 6	Gaussian, inc	https://gaussian.com
Athena	Demeter	https://bruceravel.github.io
Artemis	Demeter	https://bruceravel.github.io
Hama	Fortran	https://www.esrf.fr/

RESOURCE AVAILABILITY

Lead contact

Further information and requests for resources and reagents should be directed to and will be fulfilled by the lead contact, Shengjiong Yang (yangshengjiong@163.com).

Materials availability

This study did not generate new unique regent.

Data and code availability

- All data reported in this paper will be shared by the lead contact upon request.
- This paper dose not report original code.
- Any additional information required to reanalyze the data reported in this paper is available from the lead contact upon request.
- All datasets used to generate the results are available in the main article. Further details could be obtained from the corresponding author on reasonable request.

METHOD DETAILS

Preparation of catalysts

I-SACs were synthesized through the following procedure: iron (II) acetate tetrahydrate (62.1 mg) and 1,10-phenanthroline monohydrate (707.9 mg) were rapidly dissolved in 10 mL of ethanol, and then magnetically stirred for 20 min at 25°C to obtain a homogeneous solution. Subsequently, carbon black (2.0 g) was added to the solution, and the mixture was heated in a water bath at 80°C for 4 h under continuous stirring. The resultant was then dried at 80°C in the air for 48 h to remove residual ethanol and obtain a precursor. The precursor was further placed in a tube furnace, and pyrolyzed at 600°C for 2 h at a ramp of 10°C min^{-1} in an N_2 atmosphere to obtain I-SACs.

Characterization of catalysts

The information of phase surface and element division were collected by field emission scanning electron microscopy (FESEM, ZEISS GeminiSEM 500, GER) and high-angle annular dark-field scanning TEM (HAADF-STEM, FEI, Themis Z). X-ray diffraction (XRD) patterns for phase and crystallite analysis were

collected (10–80°, 0.02°/step, 0.05 seconds/step) by a Rigaku Ultimate IV diffractometer (Cu-Kα) at room temperature. Surface functional groups of samples were detected with a Nicolet iS50 Fourier transform infrared spectroscopy (FT-IR, Thermo Scientific, USA). ATR-FT-IR spectra were also acquired on Nicolet iS50 (Thermo Scientific, USA) with Thermo Scientific OMNIC software. X-ray photoelectron spectroscopy (XPS) were used for valent state investigation through ESCALAB 250Xi spectrometer (Thermo Scientific, USA) equipped with a pass energy of 30 eV with a power of 100 W (10 kV and 10 mA) and Al Kα X-ray ($h\nu$ = 1486.68 eV) source. N_2 adsorption-desorption isotherms of all carbon catalysts were evaluated at 77 K by a surface area and porosity analyzer V-sorb 2800 (Gold APP Instruments, China). The specific surface area (S_{BET}) was calculated according to the Brunauer-Emmett-Teller equation. The pore volume was calculated through the Barrett-Joyner-Halenda (BJH) method. Raman spectra were recorded by DXR 2xi (Thermo Scientific, USA). Electron paramagnetic resonance (EPR, Bruker EMXmicro-6/1) was used for the spinning trap experiments. The content of Fe was detected by Inductively coupled plasma mass spectrometry (ICP-MS, Agilent-7800, USA). ^{57}Fe Mössbauer spectra (MFD-500AV-02, Topologic Systems, Inc, Japan) was used to identify the valence state and spin state of Fe in catalyst. X-ray absorption fine structure (XAFS, BSRF, China) was conducted to demonstrate the existence of possible atomic structure of the samples.

Degradation of pollutions

Pollutions degradation tests were conducted in 120 mL beakers. Each pollution solutions were prepared at given concentrations and adjusted to the required pH with 0.1 M H_2SO_4 and NaOH. 10 mg of catalysts were added to the solutions and dispersed through magnetic stirring, and the water is deionized water (18.2 MΩ) from a Milli-Q system in this contribution. Different amounts of PMS were then added to the solutions to initiate the oxidation reaction. At given time intervals, 1.0 mL samples were collected, filtrated with a 0.22 μm membrane and immediately quenched with 0.5 mL methanol. The concentrations of pollutions were measured with an ultra-high-performance liquid chromatography (UHPLC, Thermo Ultimate 3000) with a diode array detector detector and a Thermoscientific syncronis C18 column (100 mm * 2.1 mm). The mobile phase, flow rate and detecting wavelength were listed in Table S4.

Electrochemical measurements

All electrochemical measurements were performed on an Electrochemical Workstation (CHI660E) through three-electrode mode. Saturated calomel electrode (saturated with 3 M KCl) was used as the reference electrode, Pt wire electrode was used as the counter electrode, and glassy carbon electrode was employed as working electrode. 100 mM Na_2SO_4 solution (100 mL) was prepared as electrolyte. Typically, catalysts (4 mg) were dispersed in 1 mL of ethanol (containing 0.03 mL of 5.0 wt % Nafion) under ultrasonic agitation to form homogeneous catalyst ink. Then 10 μL of the ink was collected and dropped on the surface of the glassy carbon electrode (5 mm diameter, 0.196 cm^2) and dried at room temperature. In Open Circuit Potential analysis.[65] Ag/AgCl electrode was used as the reference electrode.

Computations

Density functional theory (DFT) calculation was conducted by using Gaussian 16 W.1B quantum chemical software package.[66] The B3LYP-D3 method with Grimme's dispersion correction was used in the basis set of 6-31+G(d,p) for all elements.[67] Considering the negligible relativistic effect of the fourth-period transition metals, pseudo-potential for Fe was not used to better investigate electron delocalization in the coordination complexes. All atoms were free to move during geometry optimization. The edge of the carbon matrix was terminated with H atoms. The electrostatic potential, spin density, and behavior of π electrons-related orbitals were analyzed by using the Multiwfn package.[68,69]

QUANTIFICATION AND STATISTICAL ANALYSIS

Figures represented averaged or representative results of multiple independent experiments. Analyses and plots were performed with Origin.

ADDITIONAL RESOURCES

There are no additional resources needed to be declared in this manuscript, additional requests for this can be made by contacting the lead contact.